# RCS Simulation of Double S-Shaped Inlet with Radar Absorbing Materials Shedding Using Iterative Physical Optics with Impedance Boundary Condition

Xiao Guo*, Xinru Xia, Zhujun Zhao, Mengke Wu and Yu Liu

School of Aero Engine, Zhengzhou University of Aeronautics, Zhengzhou, 450046, China


**INFORMATION**

**Keywords:**
Aero-engine
S-shaped inlet
radar cross section
iterative physical optics
impedance boundary condition
shedding probability

**DOI:** 10.23967/j.rimni.2025.10.68070

SCIPEDIA Revista Internacional de Métodos Numéricos para Cálculo y Diseño en Ingeniería

Revista Internacional Métodos numéricos para cálculo y diseño en ingeniería RIMNI

In cooperation with CIMNE

# RCS Simulation of Double S-Shaped Inlet with Radar Absorbing Materials Shedding Using Iterative Physical Optics with Impedance Boundary Condition

**Xiao Guo*, Xinru Xia, Zhujun Zhao, Mengke Wu and Yu Liu**

School of Aero Engine, Zhengzhou University of Aeronautics, Zhengzhou, 450046, China

**ABSTRACT**

The inlet of an aircraft engine is a primary contributor to the aircraft's forward electromagnetic scattering. S-shaped inlet and radar absorbing materials (RAM) coatings have been widely adopted as effective measures to reduce forward radar cross section (RCS). To investigate the influence of RAM shedding on the RCS reduction efficiency, the electromagnetic scattering characteristics of the inlet under five different shedding probabilities were calculated using the iterative physical optics (IPO) combined with impedance boundary condition (IBC). Numerical simulation results demonstrate that the forward RCS of the S-shaped inlets increases monotonically with shedding probability. In the yaw plane, intact non-magnetic RAM exhibits better RCS reduction efficiency (RRE) than that in the pitch plane across all scenarios. Specifically, at a shedding probability of 0.7, the remaining non-magnetic RAM maintains an RRE exceeding 40% in the pitch plane. Collectively, these results suggest that recoating the non-magnetic RAM is recommended when the shedding probability exceeds 0.7 in either detection plane to sustain critical stealth performance.

OPEN ACCESS

**Received:** 20/05/2025

**Accepted:** 13/08/2025

**Published:** 27/10/2025

**DOI**
10.23967/j.rimni.2025.10.68070

**Keywords:**
Aero-engine
S-shaped inlet
radar cross section
iterative physical optics
impedance boundary condition
shedding probability

## 1 Introduction

Since the beginning of the 21st century, combat aircraft have been confronted with the challenge of multi-directional detection from space, air, ground and sea-based platforms. Consequently, stealth capability has emerged as a key criterion for evaluating the effectiveness of modern fighter aircraft [1,2]. Notably, the aircraft engine inlet is a prominent source of forward electromagnetic scattering, thereby playing a critical role in achieving the overall stealth of combat aircraft. Advanced inlet designs must not only optimize aerodynamic performance but also enhance stealth characteristics [3,4]. Typical technical strategies to reduce the radar cross section (RCS) of the inlet include configuring the inlet as an S-shaped duct and applying radar absorbing materials (RAM) [5].

Extensive research has been conducted on the internal flow field characteristics and electromagnetic scattering properties of S-shaped inlets. Asghar et al. [6] evaluated the internal performance of the S-shaped inlet to analyze the effects of various geometric design parameters. Their results indicated that the streamwise and circumferential pressure gradients induce three-dimensional flow

*Correspondence: Xiao Guo (guoxiao@zua.edu.cn). 

within the inlet, leading to exit-plane distortion. These findings provided critical insights for predicting engine performance during high-speed subsonic flight. Aslan and Kurtulus [7] systematically investigated the influence of different turbulence models on the computational flow characteristics of the S-shaped inlet, as well as the impact of the intake flow structures on internal flow dynamics. Their studies demonstrated that numerical simulation can effectively capture lip separation and secondary flow formation. However, they emphasized that more sophisticated turbulence modeling is required to achieve high-precision predictions of pressure recovery coefficients and distortion indices. Selvanayagam et al. [8] performed numerical simulations on S-shaped inlets integrated with Vortex Generator (VG) vanes. Their results showed that the VGs induce additional secondary flow in the duct, significantly reducing the pressure recovery and increasing the distortion coefficient at the aerodynamic interface plane (AIP). This deterioration in AIP conditions was attributed to the absence of a thick boundary layer at the inlet entrance, which amplifies the disruptive effects of secondary flow structures. Gopaliya et al. [9] analyzed the influence of momentum transfer technology on the inlet performance. They found that it enhances the static pressure recovery coefficient at the outlet while minimizing the flow non-uniformity. Wang et al. [10] developed an efficient optimization framework integrating the Kriging model and non-dominated sorting genetic algorithm-II (NSGA-II) to accelerate the design process. Their findings revealed that index DC60 decreased by a 0.24 reduction in the total pressure distortion index DC60 at the target Mach number compared to the baseline configuration, and a 2 dB decrease average RCS at 3 GHz, establishing a robust strategy for aerodynamic-electromagnetic integrated optimization of S-shaped inlet and demonstrating the feasibility of multi-objective optimization in balancing stealth and aerodynamic performance. Das et al. [11] used the computational fluid dynamics method to study the effects of inlet velocity, turning angle, and area ratio on the S-shaped diffuser, aiming to determine its optimal design and operating conditions. The results of numerical analysis show that when the turning angle increases, the transverse flow velocity becomes more significant, and the degree of flow separation decreases; when the area ratio increases, the amplitude of the in-plane flow velocity increases, and the flow separation at the bottom wall intensifies. Gil-Prieto et al. [12] used time-resolved particle image velocimetry (TR-PIV) to measure the three-component velocity field at the exit plane of a double S-shaped inlet across a range of inlet Mach numbers. Their results yielded a high-spatial-resolution, time-resolved dataset enabling detailed analysis of unsteady flow phenomena at the exits of complex aero-engine inlets. Song et al. [13] calculated the RCS of an S-shaped inlet using the shooting and bouncing ray (SBR) method. To enhance stealth, they designed a conformal inductively coupled plasma (ICP) device integrated with the inlet structure with experimental validation confirming its effective stealth enhancement. Huang et al. [14] analyzed the effects of entrance geometry on the aerodynamic performance and RCS of the Slide-Mounted inlet. Their findings indicated that an equilateral triangle entrance provided superior overall stealth, while a trapezoidal entrance offered advantages in specific angular domains. Multi-objective trade-off analysis identified the equilateral triangle entrance as optimal for balancing aerodynamic efficiency and stealth in multi-threat scenarios. He et al. [15] used a multi-objective particle swarm optimization (MOPSO) algorithm based on a radial basis function (RBF) neural network to conduct a multi-objective optimization design of the aerodynamic and electromagnetic characteristics of an S-shaped inlet with internal bosses. Two non-dominated solutions were selected from the Pareto front and their performance was compared with that of the original model and a single S-shaped inlet. Deng et al. [16] proposed an aerodynamic/stealth optimization design method for S-shaped inlets based on the discrete adjoint method. The upwind scheme was introduced into the aerodynamic adjoint equation to solve the problems of shock waves and flow separation, and the multilevel fast multipole algorithm (MLFMA) was adopted in the stealth adjoint equation. The back S-shaped inlet of the flying-wing layout was optimized to improve its

aerodynamic and stealth characteristics. The aerodynamic/stealth joint optimization increased the total pressure recovery coefficient to 0.9816, reduced the distortion index to 0.0218, and decreased the RCS to 1.2620 $m^2$.

The application of RAM in aero-engine has also been extensively studied. Choi et al. [17] proposed a novel broadband radar absorbing sandwich composite (BRASC) composed of glass fiber reinforced polymer (GFRP), a foam core, and an integrated layer of carbon nanotube (CNT) composites. The BRASC was specifically designed to minimize the RCS of inlets. Wang [18] developed a generalized equivalent model for thin coatings. Compared with the full-wave model, this equivalent model retained computational accuracy without introducing additional unknowns, thereby significantly reducing computational resource consumption. It holds potential for applications in the design and optimization of RAM-coated aero-engine inlets. Chen et al. [19] designed five absorptive material coating schemes for afterburners. Using the ray tracing method, they simulated and analyzed the impact of coating positions on the RCS distribution of the exhaust system under the S and X bands. Their findings revealed that the flame stabilizer which has been the most prominent scatterer of radar characteristic signals within the exhaust system achieved the most significant signature reduction through RAM application. Lu et al. [20] investigated the influence of RAM application positions on the integrated afterburner chamber's backward radar scattering characteristics. Their results indicated that the afterburner center cone and integrated struts exert a considerable impact on backward scattering, suggesting these components should be prioritized for radar-absorbing media application. Such findings contribute to enhancing the survivability and penetration capabilities of combat aircraft. Collectively, these studies highlight the interdependence between aerodynamic and electromagnetic properties, emphasizing the necessity of integrated design strategies to advance the performance of S-shaped inlets in combat aircraft.

The primary mechanism underlying RAM shedding is the scouring effect of high-velocity airflow during operational service. Based on literature findings [21], the dominant shedding modes of aviation-grade coated wave-absorbing materials can be classified according to their spatial distribution and occurrence pattern: local shedding and random shedding. Local shedding refers to the continuous detachment of absorbing material over a specific area at a fixed location, while random shedding involves the dislodgment of small-area absorbing material at arbitrary positions.

In summary, researchers worldwide have conducted extensive investigations on the flow dynamics and electromagnetic scattering behaviors of S-shaped inlets. However, a significant research gap remains in investigating the electromagnetic scattering characteristics of RAM-coated S-shaped inlets—particularly regarding the effects of absorbing medium shedding. To address this gap, the present work employs a hybrid methodology combining the interactive physical optics (IPO) method and impedance boundary conditions (IBC) to quantify the impact of RAM shedding on RCS reduction efficiency.

## 2 Computation Scheme

### *2.1 Interactive Physical Optics*

The IPO algorithm is an iterative numerical method for solving the electromagnetic scattering field of open-ended cavity, based on the physical optics approximation while accounting for multiple electromagnetic wave reflections between cavity walls. By using optical currents and correction currents to approximate the actual surface currents of the target, the IPO algorithm effectively overcomes the challenge posed by large cavity depths—a critical advantage when modeling complex geometries such as S-shaped inlets, where wave multi-bounce effects are prominent [22,23]. The basic calculation principle of the IPO algorithm is as follows:

$$\boldsymbol{J} = \boldsymbol{J}_0 + \boldsymbol{J}_1 \tag{1}$$

where, $\boldsymbol{J}_0$ is initial induced currents generated by physical optical method. $\boldsymbol{J}_1$ is the correction term for initial induced currents.

Fig. 1 depicts the open-ended cavity model, where Sa denotes the intake aperture surface of the cavity and Sc represents the ideal conductor wall surface. According to the electromagnetic field equivalence principle, the electromagnetic current on the inlet surface can be mathematically formulated as:

$$\boldsymbol{J}_a^i\left(\vec{r}_a\right) = \vec{n} \times \boldsymbol{H}_a^i\left(\vec{r}_a\right) \tag{2}$$

$$\boldsymbol{M}_a^i\left(\vec{r}_a\right) = \boldsymbol{E}_a^i\left(\vec{r}_a\right) \times \vec{n} \tag{3}$$

where, $\boldsymbol{J}_a^i\left(\vec{r}_a\right)$ and $\boldsymbol{M}_a^i\left(\vec{r}_a\right)$ are the equivalent current and magnetic current on the intake surface. $\vec{n}$ is the normal unit vector which is pointing into the cavity. $\boldsymbol{E}_a^i\left(\vec{r}_a\right)$, $\boldsymbol{H}_a^i\left(\vec{r}_a\right)$ are the equivalent current and equivalent magnetic current generated by the incident electromagnetic field on the intake surface.

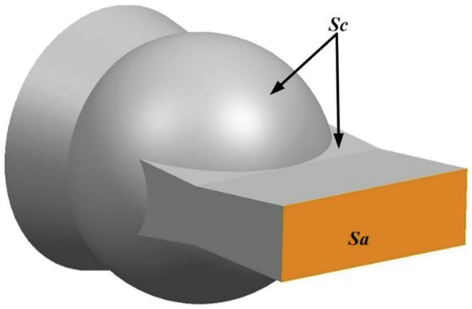


**Figure 1:** One open-ended cavity

The initial electromagnetic field generated on the inlet surface can be calculated based on the Kirchhoff formula.

$$\begin{aligned}\boldsymbol{E}_0\left(\vec{r}_c\right) \approx & \int_{Sa} \boldsymbol{M}_a^i\left(\vec{r}_a\right) \times \nabla G\left(\vec{r}_c - \vec{r}_a\right) dSa \\ & + \frac{1}{jkY}\nabla \times \int_{Sa}\left[\boldsymbol{J}_a^i\left(\vec{r}_a\right) \times \nabla \mathrm{G}\left(\vec{r}_c - \vec{r}_a\right)\right] dSa\end{aligned} \tag{4}$$

$$\begin{aligned}\boldsymbol{H}_0\left(\vec{r}_c\right) \approx & \int_{Sa} \boldsymbol{J}_a^i\left(\vec{r}_a\right) \times \nabla G\left(\vec{r}_c - \vec{r}_a\right) dSa \\ & + \frac{1}{jkY}\nabla \times \int_{Sa}\left[\boldsymbol{M}_a^i\left(\vec{r}_a\right) \times \nabla \mathrm{G}\left(\vec{r}_c - \vec{r}_a\right)\right] dSa\end{aligned} \tag{5}$$

The integral equation approach is employed to solve the magnetic field integral equation (MFIE), with the PO method providing initial values for the iterative computation and the IPO method calculating the current correction terms. The mathematical formulation for the corrective current is expressed as follows:

$$\boldsymbol{J}_N\left(\vec{r}_c\right) = \boldsymbol{J}_0 + 2\vec{n} \times P.V. \int_{Sc} \boldsymbol{J}_{N-1}\left(\vec{r}_c\right) \times \nabla G\left(\vec{r}_c - \vec{r}_c'\right) dSc \tag{6}$$

where, $P.V.$ is the main value integral symbol. $N$ represents the number of iterations. $\nabla$ represents Hamiltonian Operator. $\vec{r}_c$, $\vec{r}'_c$ are the position vector of the panel elements that are not obstructed on the wall of the cavity.

The induced current on the target surface can be calculated from Eq. (6). Also the scattering field on the intake surface can be obtained according to Kirchhoff's approximation formula:

$$\boldsymbol{E}^s\left(\vec{r}_a\right) \approx \frac{1}{jkY}\nabla \times \int_{Sc} \boldsymbol{J}\left(\vec{r}_c\right) \times \nabla G\left(\vec{r}_a - \vec{r}_c\right) dSc \tag{7}$$

$$\boldsymbol{H}^s\left(\vec{r}_a\right) \approx \int_{Sc} \boldsymbol{J}\left(\vec{r}_c\right) \times \nabla G\left(\vec{r}_a - \vec{r}_c\right) dSc \tag{8}$$

The equivalent electromagnetic field on the inlet surface can be obtained from Eqs. (7) and (8). The scattering electric field in the far-field region generated by the equivalent electromagnetic field on the intake surface can be obtained using the principle of field equivalence. To enhance the iterative computation efficiency of the IPO method, a front-back iterative scheme and relaxation factor technique are incorporated into the iterative process. The former alternates the update sequence of surface currents on different cavity regions to accelerate error convergence, while the latter introduces a weighting parameter to dampen high-frequency oscillations in the iterative solution, ensuring numerical stability.

When modeling RAM-coated cavities, the IPO algorithm incorporates the IBC to characterize the electromagnetic properties of the absorbing layer [24–26]. The IBC applies an equivalent impedance or a partial differential equation to the interface between the scatterer and the surrounding space, avoiding the analysis of complex electromagnetic waves within the coating layer, thus greatly simplifying the calculation. The IBC is primarily applicable to non-ideal conductor surfaces or conductor surfaces coated with thin dielectrics layers, establishing a simplified linear relationship between the tangential components of the electric and magnetic fields on the target surface.

The vector form of impedance boundary conditions is

$$\vec{\boldsymbol{n}} \times \boldsymbol{E} = Z_s \vec{\boldsymbol{n}} \times \vec{\boldsymbol{n}} \times \boldsymbol{H} \tag{9}$$

The impedance boundary condition $Z_s$ is generally considered to be related to incident wave angles. It can be approximated that $Z_s$ is independent of the incident angle for the RAM with a large refractive index.

$$Z_s = jZ_0\sqrt{\mu_r/\varepsilon_r}\tan\left(kt\sqrt{\varepsilon_r\mu_r}\right) \tag{10}$$

In the above formal: $\varepsilon_r$ is the relative dielectric constant. $\mu_r$ is the relative magnetic permeability. $t$ is the thickness of the RAM. $k$ is the free space wave numbers. $Z_0$ is the free space wave impedance. When the material impedance matches the free space impedance, the reflection coefficient approaches zero, resulting in the optimal wave absorption effect; conversely, the reflection coefficient increases, and the wave absorption performance deteriorates.

When combined with the IPO method, the equivalent impedance boundary condition can effectively solve the problem of coated dielectric cavities while maintaining reasonable accuracy.

The use of impedance boundaries requires meeting the following requirements:

1) The coating medium has a relatively large refractive index and loss;

2) The radius of curvature of the coating surface is much larger than the wavelength of the absorbing material;
3) On the surface of the coating material, the external field changes gently within a scale comparable to the wavelength.

To verify the calculation accuracy of the IPO algorithm combined with impedance boundary conditions proposed in this paper for the calculation of dielectric-coated cavities, numerical simulation calculations were performed on the single-ended open dielectric-coated cylindrical cavity proposed in reference [27], and comparisons were made with the experimental test values. The dimensions of the cylindrical cavity are shown in Fig. 2, with an incident angle ranging from 0° to 50° at an angle interval of 1°, and an incident frequency of 10 GHz. The electrical properties of RAM employed in the simulation are in accordance with those described in reference [27] as follows: $\mu_r = 1.0 - j0$, $\varepsilon_r = 6.11 - j0.78$. The thickness of RAM used is 0.006 m.

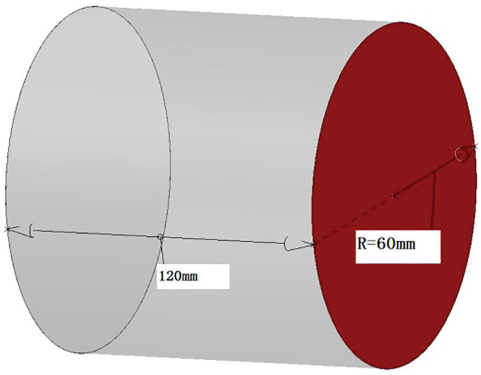


**Figure 2:** Open-ended cavity with medium coated

Fig. 3 presents the angular distribution curves of RCS from numerical calculations and experimental tests for the dielectric-coated cylindrical cavity. In this figure, "Experiment" denotes the experimental results, while "IPO" represents the numerical simulation results obtained by the IPO algorithm with IBC developed in this study. It can be observed that, under both polarization modes, within a relatively small detection angle range, the IPO-IBC method achieves excellent simulation performance for the RCS of the dielectric-coated cylindrical cavity within a relatively narrow detection angle range, with the calculated results being in good agreement with the experimental data.

### *2.2 Random Shedding Model*

In the RCS simulation of the open-ended cavity, the wall surface is discretized using unstructured meshes. For modeling RAM shedding, the surface element meshes in the coated region adopt two distinct boundary conditions: the perfect electric conductor (PEC) boundary for shed surface elements and the impedance boundary for unshed elements. To accurately reproduce the stochastic nature of RAM shedding, a random number generation function is incorporated into the processing of the coated surface meshes, which generates a random value within the interval [0, 1]. For each mesh element, if the predefined shedding probability $P_{shed}$ is less than the random number, the RAM at this location is considered intact, and the element is assigned the IBC. Conversely, if $P_{shed}$ exceeds the random number, the element is classified as shed, with the PEC boundary condition applied. Mathematically, this model is formalized as:

For element $i$: $\begin{cases} \text{Impedance boundary} & \text{if } P_{shed} < \xi_i \\ \text{PEC boundary} & \text{if } P_{shed} \geq \xi_i \end{cases}$

where $\xi_i \sim U(0,1)$ is the uniformly distributed random number for element $i$.

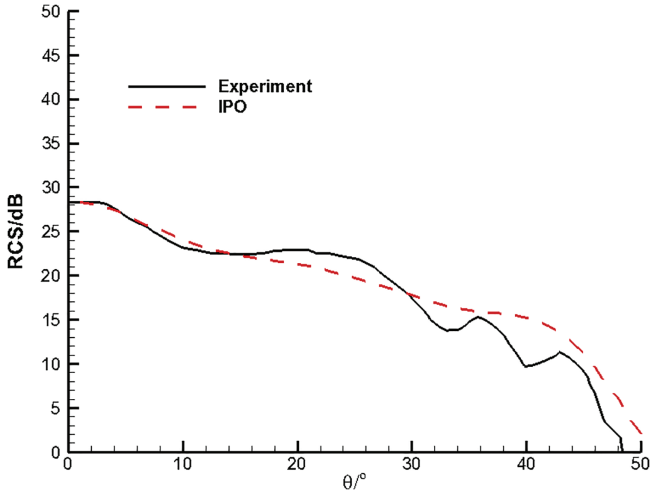


**Figure 3:** Numerical calculation and experimental test of RCS curve

### *2.3 Designed Coating Scheme*

Fig. 4 illustrates the regional division of the S-shaped inlet. The S-shaped inlet with RAM coating on region C, D, and E is assumed as the reference model without RAM shedding. To systematically analyze the effects of shedding, the shedding probability $P_{shed}$ is varied from 0.1 to 0.9 in increments of 0.2, representing low to high levels of material loss severity. The electrical properties of RAM employed in the simulation are specified as follows: $\mu_r = 1.0 - j0$, $\varepsilon_r = 6.11 - j0.78$. The thickness of RAM is 0.006 m.

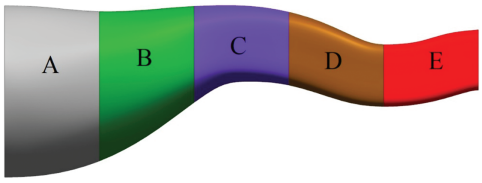


**Figure 4:** The regional division diagram

### *2.4 RCS Reduction Efficiency*

The RCS reduction efficiency (RRE) is a key metric for quantifying the stealth enhancement provided by RAM. It mathematically characterizes the effectiveness of absorbing materials in reducing electromagnetic scattering, defined as:

$$RRE = \left| \frac{\sigma_n - \sigma_0}{\sigma - \sigma_0} \right| \tag{11}$$

In the above form, $\sigma_0$ is the average RCS value of the S-shaped inlet without RAM coated. $\sigma$ is the average RCS value of the S-shaped inlet with RAM coated which is not falling off. $\sigma_n$ is the average

RCS value of the S-shaped inlet with RAM coated which is falling off under the different shedding probability.

## 3 Presentation of Results

Fig. 5 shows detection angles of incident electromagnetic waves, spanning from –30° to 30° in the pitch plane and 0° to 30° in the yaw plane, with both intervals incremented at 1°. This configuration comprehensively covers typical radar threat sectors encountered by aircraft in forward-facing scenarios. The incident wave is set to a frequency of 10 GHz, corresponding to the X-band widely used in airborne and ground-based radar systems. The wall surface is discretized using an unstructured triangular grid, with the surface mesh size $\lambda/9$ determined based on the requirements of the IPO algorithm. The total number of mesh elements is 45,756. A program implemented in C language was used to integrate the IPO method with IBC for numerical analyses, and all the data were processed and plotted using Tecplot.

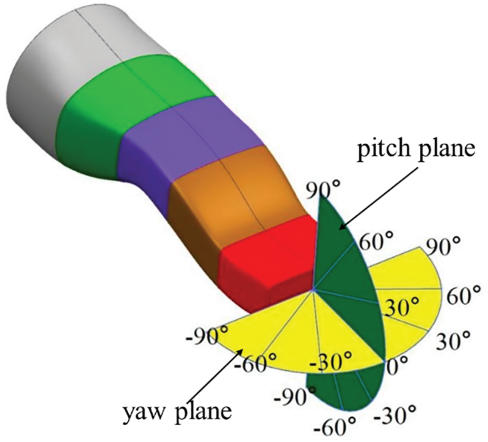


**Figure 5:** The detection angle setting diagram

Fig. 6 shows the RCS curves of the S-shaped inlet under the horizontal polarization in the pitch plane. Three distinct RCS angular distribution patterns are observed under horizontal polarization. When $P_{shed} < 0.5$, the phase difference between the peaks and valleys of RCS curve remains minimal, with small amplitude variations across the detection range. This indicates that minor RAM shedding causes negligible disruption to the electromagnetic wave absorption and scattering cancellation mechanisms. However, when $P_{shed} > 0.5$, significant deviations in both RCS amplitude and angular distribution emerge within the $-20°$ to 10° and 20° to 30° sectors compared to the intact RAM case. The maximum difference in RCS amplitude can reach 25 dBsm at specific angles, highlighting the critical role of RAM integrity in maintaining stealth performance. Within these two detection angle ranges, the main reason for the increase in the RCS amplitude of the inlet when the shedding probability is greater than 0.5 is primarily due to the direct illumination of the upper surface of Part D and Part E. Even partial shedding exposes underlying PEC surfaces, causing specular reflections that dominate the scattering field. The coherent superposition of these reflections with diffracted waves from the inlet's S-bend structure exacerbates RCS elevation in this forward-facing sector, which is critical for head-on radar detection scenarios.

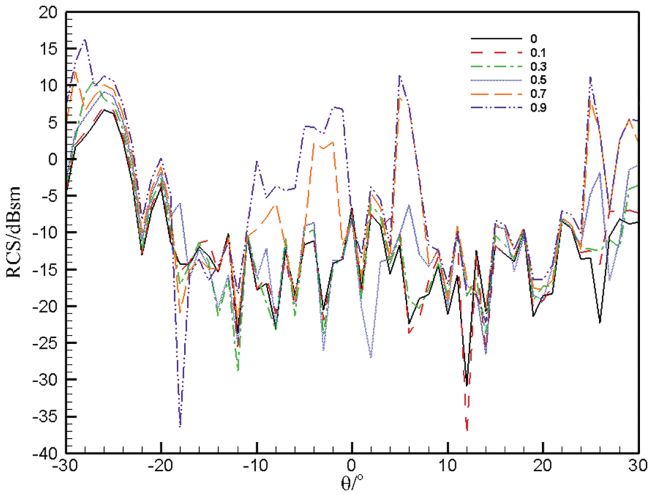


**Figure 6:** RCS curves of the S-shaped inlet under the horizontal polarization in the pitch plane

Fig. 7 presents the RCS curves of the S-shaped inlet under vertical polarization in the pitch plane. As observed, the RCS amplitude increases monotonically with shedding probability $P_{shed}$, with the primary impact concentrated on amplitude rather than phase. Within the $-30°$ to $0°$ range, direct illumination of RAM-shed areas which are modeled as PEC conditions disrupts the incident wave's energy distribution, causing specular reflections that elevate RCS. For $P_{shed} > 0.7$, the RCS angular pattern diverges significantly from that of lower shedding scenarios within $10°$ to $20°$ range. In this range, the incident electromagnetic wave illuminates the bulge area of the inlet. The reflected wave, shaped by the region's geometry, propagates in multiple directions. This reflected wave subsequently irradiates the non-shedding regions, altering the energy distribution and propagation path of the electromagnetic waves.

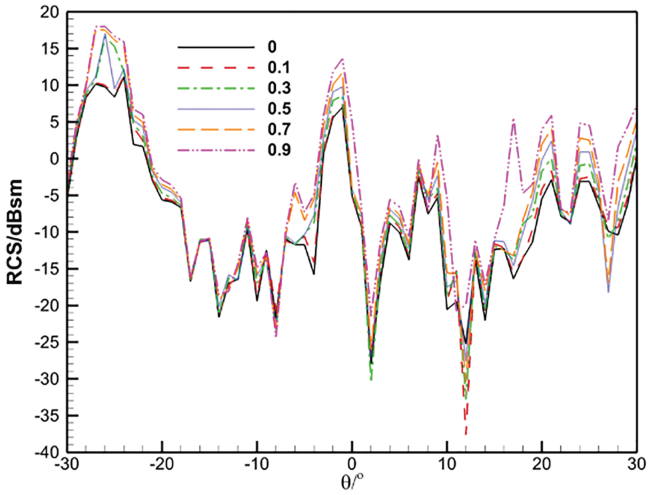


**Figure 7:** RCS curves of the S-shaped inlet under the vertical polarization in the pitch plane

Fig. 8 presents the RCS curves of the S-shaped inlet under two polarizations in the yaw plane. RAM shedding exerts a subtle yet systematic impact on both RCS amplitude and angular distribution

in this plane. At most detection angles, RCS increases with the shedding probability $P_{shed}$. Notably, larger RCS amplitudes are observed at specific angles, such as $\theta = 7°$, 15° and 22°, potentially attributed to the uneven distribution of incident electromagnetic energy caused by random RAM shedding. As shown in Fig. 8b, when $P_{shed} = 0.9$, the RCS angular distribution differs significantly from other scenarios within the 0° to 10° detection range. This discrepancy arises because RAM coated on the surfaces of Parts C, D, and E is nearly completely shed off under this high shedding probability. Compared with results in the pitch plane, the RCS amplitude difference caused by the varying shedding probabilities is smaller in the yaw detection plane. This is primarily due to the focuses on a two-dimensional inlet: in the yaw plane, the area directly irradiated by incident electromagnetic waves is smaller, thereby reducing the influence of RAM shedding.

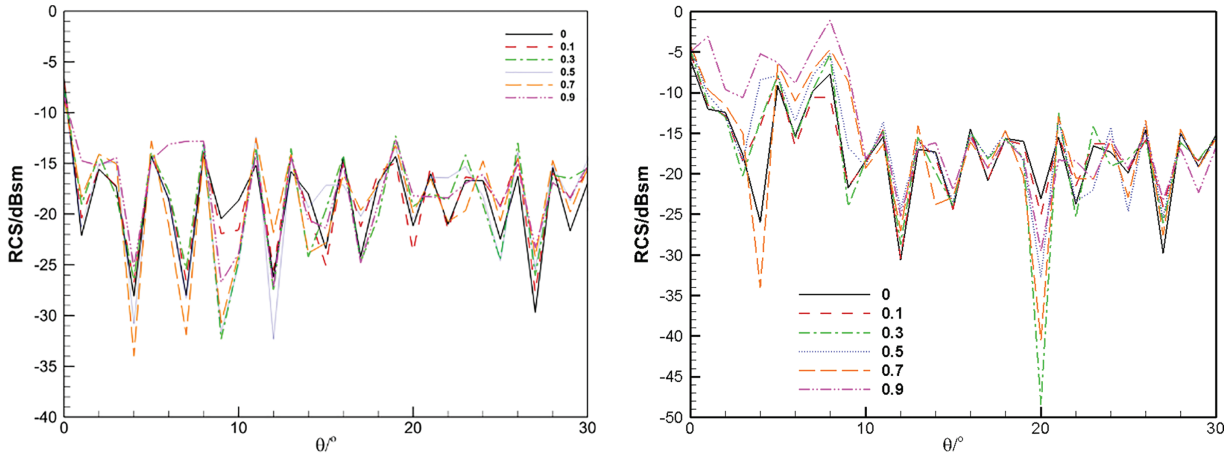


**Figure 8:** RCS curves of S-shaped inlet in the yaw plane. (a) Horizontal polarization; (b) Vertical polarization

Fig. 9 presents the induced current distribution at $\theta = 0°$ under the horizontal polarization in the pitch plane. As shown, when $P_{shed} = 0.3$, a primary high-density current region first emerges on the upper surface of Part B. As $P_{shed}$ increases to 0.5, a secondary high-density induced current region appears on the lower surface of Part C. The spatial extent of these high-density current regions expands monotonically with increasing $P_{shed}$, reflecting enhanced electromagnetic wave interaction with exposed PEC surfaces due to RAM shedding.

Fig. 10 presents the current distribution at $\theta = 10°$ under the vertical polarization in the yaw plane. As shown, a persistent high-density induced current region is observed in Part E, with the current density in this area increasing monotonically with shedding probability $P_{shed}$. When $P_{shed} = 0.7$, a secondary high-density induced current region emerges on the lower surface of Part C. Although RAM shedding does not alter the overall propagation path of electromagnetic waves, random shedding events modify the energy distribution of waves upon reflection from the cavity walls, leading to localized enhancements in current density at exposed PEC interfaces.

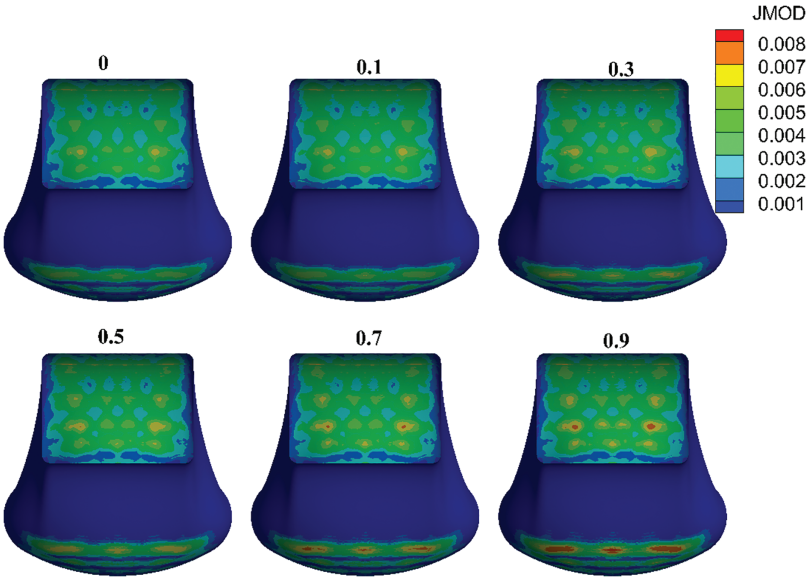


**Figure 9:** Induced current distribution at $\theta = 10^{o}$ under the horizontal polarization in the pitch plane (unit: mA/m$^2$)

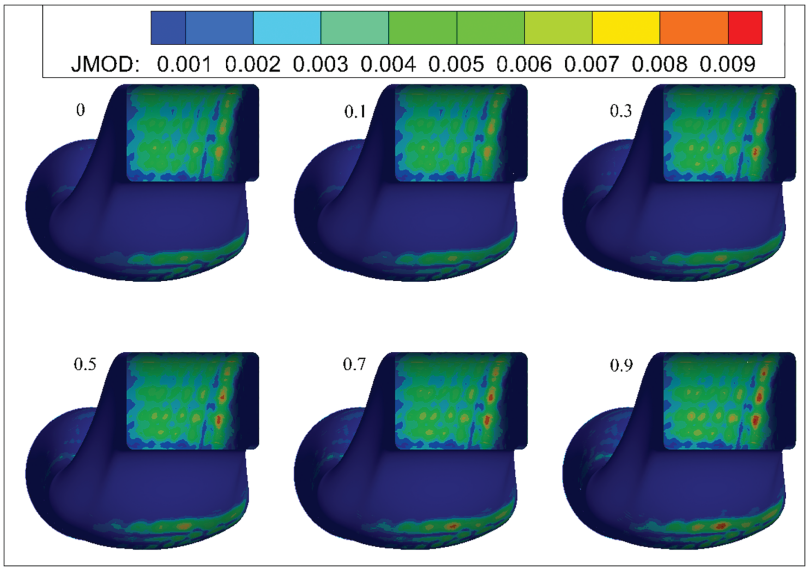


**Figure 10:** Induced current distribution at $\theta = 10^{o}$ under the vertical polarization in the yaw plane (unit: mA/m$^2$)

Table 1 presents the mean RCS and RRE for two polarizations across the pitch and yaw planes, with the RRE of the intact RAM model (no shedding) normalized to 100%. As shown in the table, the mean RCS of the shedding model consistently exceeds that of the reference model, increasing monotonically with shedding probability $P_{shed}$. RAM exhibits a more pronounced RCS reduction effect under horizontal polarization than under vertical polarization across both detection planes. Notably, when $P_{shed} > 0.5$, the RRE under horizontal polarization of the pitch plane declines sharply, while it

remains below 50% under vertical polarization. In contrast, the RRE under horizontal polarization of the yaw plane remains above 80% across all shedding probabilities, retaining approximately 50% efficiency even at $P_{shed} = 0.9$. The impact of RAM shedding on the RCS in the yaw plane is relatively minor, which is attributed to the lower energy of incident electromagnetic waves in yaw incidence scenarios, thereby mitigating the influence of the exposed PEC surfaces. RRE can serve as a criterion for determining the necessity of RAM repair. When $P_{shed} > 0.5$, repair should be considered to maintain stealth performance.

**Table 1:** Average RCS and RCS reduction efficiency of the S-shaped inlet (unit: $m^2$)

| | Pitch plane | | | | Yaw plane | | | |
|---|---|---|---|---|---|---|---|---|
| | Horizontal polarization | | Vertical polarization | | Horizontal polarization | | Vertical polarization | |
| Shedding probability | Average RCS | RRE | Average RCS | RRE | Average RCS | RRE | Average RCS | RRE |
| 0 | 0.348258 | 100% | 1.132879 | 100% | 0.023643 | 1 | 0.038931 | 1 |
| 0.1 | 0.39404 | 98.64% | 1.230494 | 98.24% | 0.024732 | 95.80% | 0.039593 | 99.50% |
| 0.3 | 0.680495 | 90.16% | 2.430988 | 76.55% | 0.025929 | 91.18% | 0.048922 | 92.38% |
| 0.5 | 0.620161 | 91.95% | 2.315206 | 78.64% | 0.024938 | 95.01% | 0.057773 | 85.63% |
| 0.7 | 1.495419 | 66.04% | 4.181165 | 44.94% | 0.024222 | 97.77% | 0.0628 | 81.79% |
| 0.9 | 2.941339 | 23.23% | 5.166041 | 27.14% | 0.027064 | 86.80% | 0.107252 | 47.88% |

## 4 Conclusions

The electromagnetic scattering characteristics of an S-shaped inlet with five shedding probabilities were computed using the IPO method combined with the IBC. The key findings are as follows:

(1) The forward RCS of the S-shaped inlet increases monotonically with the shedding probability $P_{shed}$, while RAM shedding has a negligible impact on the angular distribution of the forward RCS.

(2) In the pitch plane, the intact RAM exhibits superior RCS reduction efficiency under horizontal polarization compared to vertical polarization. Specifically, at $P_{shed} = 0.7$, the remaining RAM retains an RRE exceeding 40%.

(3) In the yaw plane, adhered RAM maintains higher RRE than in the pitch plane across all shedding scenarios. Collectively, these results suggest that RAM recoating is recommended to repair when $P_{shed} > 0.7$ in either the pitch or yaw plane to sustain critical stealth performance.

**Acknowledgement:** Not applicable.

**Funding Statement:** The work was supported by the National Natural Science Foundation of China (62341125), the key project of the Education Department of Henan Province, China (25A590003), the Training Program for Young Backbone Teachers in Higher Education Institutions of Henan Province, the program of the Innovation Research Team of Sci-tech, Henan Province (25IRTSTHN020) and the Scientific Research Team Plan of Zhengzhou University of Aeronautics (23ZHTD01004), and partly support by the key project of the Education Department of Henan Province, China (25A590006, 26A580005), the Key Science and Technique R&D Program of Henan Province, China (252102220016,

252102220085, 252102240134), the Open Funding of Henan Key Laboratory of General Aviation Technology (ZHKF-240207) and the Talent Support Program of Henan Province (254000510003). The authors also wish to thank them for their financial support.

**Author Contributions:** The authors confirm contribution to the paper as follows: Conceptualization, Xiao Guo; methodology, Xiao Guo; software, Xiao Guo and Xinru Xia; validation, Xinru Xia and Zhujun Zhao; data curation, Xinru Xia and Mengke Wu; writing—original draft preparation, Xiao Guo; writing—review and editing, Zhujun Zhao and Yu Liu; funding acquisition, Xiao Guo. All authors reviewed the results and approved the final version of the manuscript.

**Availability of Data and Materials:** The datasets generated and analyzed during the current study are available from the corresponding author on reasonable request.

**Ethics Approval:** Not applicable.

**Conflicts of Interest:** The authors declare no conflicts of interest to report regarding the present study.

## References

1. Cheng RH, Zhang ZS, Ruan WB, Wang JF. Core key technologies of advanced aircraft engine. Acta Aeronautica et Astronautica Sinica. 2024;46(12):6–31. (In Chinese).
2. Fan H, Duan P, Yuan C. Disruptive technologies in aviation: preliminary study. Acta Aeronautica et Astronautica Sinica. 2024;45(5):529893. (In Chinese). doi:10.7527/S1000-6893.2023.29893.
3. Sang JH. Low-observable technologies of aircraft. Beijing, China: Aviation Industry Press; 2013. 57 p. (In Chinese).
4. Madai A, Nili-Ahmadabadi M, Kermani MJ. Quasi-3D inverse design of S-shaped diffuser with specified cross-section distribution; super-ellipse, egg-shaped, and ellipse. Inverse Probl Sci Eng. 2021;29(13):2611–28. doi:10.1080/17415977.2021.1943382.
5. Huang HX, Sun S, Yu H, Tan HJ, Lin ZK, Li ZJ, et al. Recent progress in subsonic S-shaped inlets. J Propul Technol. 2020;41(12):2641–58. doi:10.13675/j.cnki.tjjs.200493.
6. Asad A, Robert A, William DE, Derrick A. Performance evaluation of an S-duct diffuser of a flight-vehicle inlet in high-subsonic flow. In: Turbo Expo: Power for Land, Sea, and Air; 2015 Jun 15–19; Montreal, QC, Canada: American Society of Mechanical Engineers. doi:10.1115/gt2015-43740.
7. Aslan S, Kurtulus DF. Numerical investigation of an S-duct diffuser at different inlet boundary conditions. Advan Sustain Aviat. 2018;50(1):111–28. doi:10.1007/978-3-319-67134-5_8.
8. Selvanayagam J, Aliaga C, Stokes J. Numerical simulation of an aircraft engine intake S-duct diffuser. In: 53rd AIAA/SAE/ASEE Joint Propulsion Conference; 2017; Atlanta, GA, USA: AIAA Propulsion and Energy Forum.
9. Gopaliya MK, Jain P, Kumar S, Yadav V, Sumit S. Performance improvement of S-shaped diffuser using momentum imparting technique. IOSR J Mech Civil Eng. 2014;11(3):23–31. doi:10.9790/1684-11312331.
10. Wang B, Wang Q. Numerical investigation of aerodynamic and electromagnetic performances for S-duct caret intake with boundary-layer bleed system. Int J Aerosp Eng. 2023;2023:1194655. doi:10.1155/2023/1194655.
11. Das AK, Singh RK, Roy M, Kumar A, Rana SC, Ansu AK, et al. Optimum design of S-shaped diffuser by studying the effect of inlet velocity, turning angle and area ratio. Int J Interact Des Manuf. 2023;17(10):2673–85. doi:10.1007/s12008-022-01132-4.
12. Gil-Prieto D, Zachos PK, Macmanus DG, McLelland G. Unsteady characteristics of S-duct intake flow distortion. Aerosp Sci Technol. 2019;84(6):938–52. doi:10.1016/i.ast.2018.10.020.

13. Song Z, Xu J, Wei X, Chen Z. Research on electromagnetic scattering and plasma stealth design of S-shaped inlet. In: 2017 Progress in Electromagnetics Research Symposium-Spring (PIERS), 2017 May 22–25; St Petersburg, Russia: IEEE; p. 2412–8.
14. Huang A, Zhan F, Sheng S. Electromagnetic scattering and aerodynamic characteristics of the side-mounted inlet. Comput Simul. 2024;41(9):13–7. (In Chinese). doi:10.3969/j.issn.1006-9348.2024.09.004.
15. He YB, Yang QZ, Shi YQ, Shi YQ, Gao X, Yang HC. Multi-objective optimization design of S-shaped inlet with internal bump. Aerosp Sci Technol. 2022;130(6):107901. doi:10.1016/j.ast.2022.107901.
16. Deng J, Zhao K, Zhou L, Zhang W, Shu B, Huang J, et al. Aerodynamic/stealth design of S-duct inlet based on discrete adjoint method. Appl Math Mech. 2024;45(4):725–46. doi:10.1007/s10483-024-3106-7.
17. Choi W-H, Kim T-I, Lee W-J. Broadband radar absorbing sandwich composite with stable absorption performance for oblique incidence and its application to an engine duct for RCS reduction. Adv Compos Mater. 2021;3(1):76–90. doi:10.1080/09243046.2020.1767882.
18. Wang MY. Electromagnetic scattering analysis of thin dielectric-coated targets [dissertation thesis]. Xi'an, China: Xidian University; 2018. (In Chinese).
19. Chen H, Li Z, Deng H, Yang S, Wang X, Wang Q. Influence of afterburner coated with absorbing material on radar scattering characteristics of engine exhaust system. Aero Weaponry. 2023;30(6):89–95. (In Chinese). doi:10.12132/ISSN.1673-5048.2023.0052.
20. Lu H, Shang S, Sun X, Wang Q, Deng HW, Li F. Influence of coating position of radar absorbing medium in the integrated afterburner on radar scattering characteristics of aeroengine. Aeroengine. 2024;50(4):68–74. (In Chinese) . doi:10.13477/j.cnki.aeroengine.2024.04.009.
21. Qiao Y, Zang Y, Yi W. Analysis on the causes of stealthy absorbing peeling off aluminum alloys surface. J Acad Armored Force Eng. 2009;23(6):84–6. doi:10.3969/j.issn.1672-1497.2009.06.020.
22. Yoo JU, Koh I. Comparison of linear iteration schemes to improve the convergence of iterative physical optics for an impedance scatterer. J Electromagn Eng Sci. 2023;23(1):78–80. doi:10.26866/jees.2023.1.l.12.
23. Shah MA, Tokgöz Ç, Salau BA. Radar cross section prediction using iterative physical optics with physical theory of diffraction. IEEE Trans Antennas Propag. 2022;70(6):4683–90. doi:10.1109/TAP.2021.3137202.
24. Melenk JM, Sauter SA. Wavenumber-explicit hp-FEM analysis for maxwell's equations with impedance boundary conditions. Found Comput Math. 2024;24(5):1871–939. doi:10.1007/s10208-023-09626-7.
25. Daveau C, Aubakirov A, Oueslati S, Carre C. Boundary element method with high order impedance boundary condition for Maxwell's equations. Appl Math Model. 2023;118(1):53–70. doi:10.1016/j.apm.2022.12.039.
26. Yuferev SV, Ida N. Surface impedance boundary conditions: a comprehensive approach. Boca Raton, FL, USA: CRC Press; 2018. doi:10.1201/9781315219929.
27. Luo W. nvestigations of the fast hybrid methods for scattering characteristics of three-dimensional electrically large complex cavity [dissertation thesis]. Chengdu, China: University of Electronic Science and Technology of China; 2008. (In Chinese).